PHYSICAL REVIEW B **97**, 155136 (2018)

Nonthermal switching of charge order: Dynamical slowing down and optimal control

Michael Schüler, Yuta Murakami, and Philipp Werner
Department of Physics, University of Fribourg, 1700 Fribourg, Switzerland

(Received 14 December 2017; revised manuscript received 6 April 2018; published 17 April 2018)

We investigate the laser-induced dynamics of electronically driven charge-density-wave (CDW) order. A comprehensive mean-field analysis of the attractive Hubbard model in the weak-coupling regime reveals ultrafast switching and ultrafast melting of the order via a nonthermal pathway. The resulting nonequilibrium phase diagram exhibits multiple distinct regimes of the order parameter dynamics upon increasing field strength, indicative of multiple dynamical phase transitions. Using an intuitive pseudospin picture, we show how the distinct dynamical regimes can be connected to the spin precession angle. We furthermore study the effects of electron-electron interactions beyond mean field to show that the main features of the phase diagram are robust against scattering or thermalization processes. For example, the nonthermal state with switched order is characterized by a particularly slow relaxation. The nonthermal phases can be stabilized by tailoring the pulse shape with optimal control theory. We also demonstrate how the dynamics allows to distinguish an electron-electron interaction driven CDW from an electron-phonon interaction driven CDW.

DOI: 10.1103/PhysRevB.97.155136

I. INTRODUCTION

The field of ultrafast coherent control of symmetry-broken phases in condensed matter has experienced a surge of research activity. Important examples include the transient enhancement of superconductivity (SC) [1–9], light-controlled order of excitonic condensates [10–13], or the transient manipulation of spin [14,15], orbital [16] and charge order [17–20]. Since charge-density-wave (CDW) order directly couples to external electric fields, it provides an ideal platform for inducing and tracing photoinduced phase transitions. Several recent experiments have addressed the mechanism behind the CDW-to-metal transition by ultrashort laser pulses. If the CDW originates from a Peierls-type lattice distortion, the light-induced melting of the order is accompanied by coherent phonon excitations [14,16–18,21,22]. In contrast, a CDW induced by electron-electron (e-e) correlations can be melted on the femtosecond timescale [10,23–25], and nonthermal melting has been observed [10,25]. These developments have stimulated intensive theoretical research of the laser-driven CDW dynamics [19,26–31]. Furthermore, since CDW and spin-density wave ordering is typically competing with SC in unconventional superconductors [32], the suppression of these orders provides a route to light-induced SC [33].

From a fundamental perspective, universal features in the time evolution of ordered states are attracting great interest. The dynamics after a generic excitation can exhibit qualitative changes—such as transitions from transiently trapped to vanishing order—beyond some critical excitation strength which cannot be explained in terms of the total energy of the system within an equilibrium picture. Such dynamical phase transitions [34–36] have been studied for various kinds of ordered phases such as superconductors [37–40], excitonic insulators [13], antiferromagnetic [41–43], ferromagnetic [36,44,45], and bosonic [46] systems.

Here we show that the e-e correlation-driven CDWs excited with short pulses can also exhibit such dynamical phase transitions. In contrast to the usual quench scenario, we identify *multiple* regimes of ultrafast nonthermal melting or switching depending on the pulse strength. We present a corresponding *nonequilibrium phase diagram* (NEPD) which reveals nonthermal slowing down and long-lived nonthermal states despite increased energy absorption. We provide an intuitive understanding of the switching and melting behavior based on time-dependent mean-field (MF) theory and a pseudospin picture. In addition, by taking e-e scattering into account at the local second-Born level, we demonstrate that the qualitative features identified in the MF dynamics are also present in a more sophisticated description, which captures thermalization effects. To access these interesting transient states efficiently, we employ quantum optimal control theory (QOCT) [47–49], which provides optimized laser pulses for either switching or suppressing the CDW order. By simultaneously minimizing the absorbed energy, we can suppress heating effects and stabilize the nonthermal states.

We also discuss the case of cooperative e-e and phonon-driven CDW order and demonstrate that the distinct nonequilibrium features of the e-e–driven CDW persist for small electron-phonon (e-ph) coupling. In contrast, dominant e-ph interactions suppress the dynamical phase transitions. The nonequilibrium dynamics hence provides a clear fingerprint of CDW order driven by e-e correlations.

The paper is organized as follows. Section II describes the model and mean-field formalism as well as the nonequilibrium Green's function approach used in this study. The results for the e-e–driven CDW are presented in Sec. III, while those for the electron-phonon system are discussed in Sec. IV. Conclusions are drawn in Sec. V.

©2018 American Physical Society

II. MODEL AND FORMALISM

In this work, we focus on the attractive Hubbard model at half filling,

$$\hat{H} = -J_0 \sum_{\langle ij \rangle,\sigma} \hat{c}^\dagger_{i\sigma}\hat{c}_{j\sigma} + \frac{U}{2}\sum_i \left(\hat{n}_{i\sigma} - \frac{1}{2}\right)\left(\hat{n}_{i\bar{\sigma}} - \frac{1}{2}\right), \quad (1)$$

where $\langle ij \rangle$ denotes nearest neighbors, U is the on-site interaction, and $\hat{n}_{i\sigma} = \hat{c}^\dagger_{i\sigma}\hat{c}_{i\sigma}$. This model describing CDW and SC order [40,50,51] and its experimental realizations in cold atom systems has recently shed new light on the dynamics of charge and spin fluctuations [52–55].

The initial state of the system is a CDW, which is characterized by a broken symmetry between neighboring sublattice sites with order parameter $\Delta n = \langle \hat{n}_\mathrm{A} \rangle - \langle \hat{n}_\mathrm{B} \rangle$. In what follows we focus on the weak-coupling regime and treat a one-dimensional (1D) configuration to simplify the numerical calculations, having in mind a quasi-1D system embedded in higher dimensions. We have confirmed that qualitatively similar results can be obtained for a two-dimensional configuration with anisotropic hopping, see Appendix D.

In momentum space, the kinetic term of the Hamiltonian (1) reads $\hat{H}_\mathrm{kin} = \sum_{k,\sigma} \varepsilon_k \hat{c}^\dagger_{k\sigma}\hat{c}_{k\sigma}$ with the free band structure $\varepsilon_k = -2J_0 \cos(ka)$ (lattice constant a). The time-dependent external laser fields, described by the vector potential $A(t)$, are incorporated by the Peierls substitution $\varepsilon_k(t) = \varepsilon_{k-A(t)}$. In what follows, we measure energies in units of J_0 [56], while k is given in units of a^{-1}. The Brillouin zone (BZ) is thus given by BZ $= [-\pi,\pi]$. We use the e-e interaction $U = -2$, which corresponds to the weak-coupling regime. Throughout this work, we focus on the paramagnetic case since spin-polarized solutions correspond to higher-energy states.

A. Mean-field treatment

First we introduce the time-dependent MF dynamics, which provides valuable insights into the short-time dynamics of the CDW system. Within the MF approximation, the time-dependent Hamiltonian (1) is replaced by

$$\hat{H}^\mathrm{MF}(t) = \sum_{k\in \mathrm{BZ}'}\sum_\sigma \hat{\mathbf{c}}^\dagger_{k\sigma}\,\widetilde{\mathbf{h}}^\mathrm{MF}(k,t)\hat{\mathbf{c}}_{k\sigma}, \quad (2)$$

where $\hat{\mathbf{c}}_{k\sigma} = (\hat{c}_{k\sigma},\hat{c}_{k+Q,\sigma})$ denotes the fermionic operators with respect to the momentum pair $(k,k+Q)$. To allow for CDW order, we have introduced the nesting vector $Q = \pi$, which leads to nested bands and a reduced Brillouin zone BZ$' = [-\pi/2,\pi/2]$, which corresponds to a doubled unit cell in real space. The effective single-particle Hamiltonian is given by

$$\widetilde{\mathbf{h}}^\mathrm{MF}(k,t) = \begin{pmatrix} \varepsilon_k(t) & \frac{U}{2}\Delta n(t) \\ \frac{U}{2}\Delta n(t) & \varepsilon_{k+Q}(t) \end{pmatrix}. \quad (3)$$

The time-dependent MF equations are solved in two steps. First, the one-body density matrix in thermal equilibrium $\boldsymbol{\rho}_\mathrm{eq}(k)$ is self-consistently computed by diagonalizing Eq. (2) and calculating the order parameter

$$\Delta n = \frac{1}{N_k}\sum_{k\sigma} \langle \hat{c}^\dagger_{k+Q,\sigma}\hat{c}_{k\sigma} \rangle \quad (4)$$

(N_k is the number of k points in the reduced BZ), until convergence is reached. Using $\boldsymbol{\rho}(k,t=0) = \boldsymbol{\rho}_\mathrm{eq}(k)$ as the initial condition, the time evolution is determined by the time stepping $\boldsymbol{\rho}(k,t+\Delta t) = \mathbf{U}_k(t+\Delta t,t)\boldsymbol{\rho}(k,t)\mathbf{U}^\dagger_k(t+\Delta t,t)$. Here, $\mathbf{U}_k(t+\Delta t,t)$ denotes the time evolution operator of the MF Hamiltonian, which is computed by fourth-order commutator-free matrix exponentials [57].

To better understand how the CDW can be manipulated by applying laser pulses, we introduce the pseudospin representation $\hat{S}^\alpha_{k\sigma} = \hat{\mathbf{c}}^\dagger_{k\sigma}\hat{\sigma}^\alpha\hat{\mathbf{c}}_{k\sigma}/2$ (Pauli matrices $\hat{\sigma}^\alpha$) with $\hat{\mathbf{c}}_{k\sigma} = (\hat{c}_{k\sigma},\hat{c}_{k+Q,\sigma})$. This concept has provided an intuitive picture of related problems [13,43,58–60]. Note that the pseudospin encodes the sublattice structure, while the physical spin need not be treated explicitly in the paramagnetic case. The particle-hole symmetry at half filling guarantees that the MF Hamiltonian (2) can be expressed in terms of pseudospin operators. The CDW order parameter in the pseudospin representation is given by

$$\Delta n = \frac{1}{N_k}\sum_{k,\sigma}\langle \hat{S}^x_{k\sigma} \rangle. \quad (5)$$

The current between the sublattice sites is, on the other hand, related to $\langle \hat{S}^y_{k\sigma} \rangle$. CDW order corresponds to a finite total pseudospin projection in the x direction, while the normal state in equilibrium consists of spins along the z direction.

With these definitions, the MF Hamiltonian and the corresponding equation of motion is cast into the simple form

$$\hat{H}^\mathrm{MF}(t) = \sum_{k\sigma} \mathbf{B}_k(t)\cdot\hat{\mathbf{S}}_{k\sigma}, \quad \frac{d}{dt}\hat{\mathbf{S}}_{k\sigma} = \mathbf{B}_k(t)\times\hat{\mathbf{S}}_{k\sigma}, \quad (6)$$

where the momentum-dependent pseudomagnetic field is given by $B^x_k(t) = U\Delta n(t)$, $B^y_k = 0$, and $B^z_k(t) = \varepsilon_k(t) - \varepsilon_{k+Q}(t)$.

Note that the MF dynamics described by the MF Hamiltonian (2) or, equivalently, the pseudospin representation (6), are expressed in terms of the momentum pair basis $(k,k+Q)$. One can also work in the basis given by the sublattice sites A, B. This is particularly convenient for formulating consistent approximations to the e-e interactions beyond the MF level, which is discussed below. The relation of both basis representations is detailed in Appendix A.

B. Nonequilibrium Green's function approach

Albeit the MF treatment discussed in Sec. II A provides a clear picture on how to understand and manipulate the CDW in the model, it ignores the effects of e-e scattering. The e-e interactions provide a mechanism for thermalizing the laser-excited system, which can suppress the order if the injected energy exceeds the threshold of the ordered state. These heating effects, which are often ignored in theoretical studies, deserve proper attention in the discussion of light-controlled order [7].

To address this, we employ a description in terms of nonequilibrium Green's functions (NEGF) [61,62]. The single-particle Green's function (GF) is defined as $\mathbf{G}_\sigma(k;z,z') = -\mathrm{i}\langle \mathcal{T}\hat{\mathbf{c}}_{k\sigma}(z)\hat{\mathbf{c}}^\dagger_{k\sigma}(z') \rangle$, where the arguments z, z' refer to the Matsubara-Keldysh contour $\mathcal{C}$, and $\mathcal{T}$ denotes the contour ordering operator. Given some approximation to the self-energy $\boldsymbol{\Sigma}_\sigma(k;z,z')$, which describes the many-body effects beyond MF, the Kadanoff-Baym equations (KBEs) yield the interacting time-dependent GF from which the relevant observables can be extracted.

In practice, the self-energy is expressed as a diagrammatic series. Since the e-e interactions are weak in our setup, the second-order (second-Born, 2B) approximation to the self-energy should yield an accurate description. It is defined by

$$\Sigma_{ij\sigma}(z,z') = U^2 G_{ij\sigma}(z,z') G_{ij\bar{\sigma}}(z,z') G_{ji\bar{\sigma}}(z',z) \tag{7}$$

in the original lattice representation and in its full generality incorporates momentum-dependent scattering processes. For low-dimensional systems, however, the available phase space is strongly restricted and the e-e scattering is strongly suppressed. For numerical simplicity and to partially reflect that the system is embedded in higher dimensions, we employ the local 2B (2Bloc) approximation. For convenience, we employ the sublattice site basis (see Appendix A) for representing the self-energy. Switching to k space, the 2Bloc is cast into a momentum-independent self-energy,

$$\Sigma_{\alpha\alpha\sigma}(z,z') = U^2 \mathcal{G}_{\alpha\alpha\sigma}(z,z') \mathcal{G}_{\alpha\alpha\bar{\sigma}}(z,z') \mathcal{G}_{\alpha\alpha\bar{\sigma}}(z',z), \tag{8}$$

where the index α refers to the sublattice site basis and

$$\mathcal{G}_{\alpha\beta\sigma}(z,z') = \frac{1}{|\mathrm{BZ}'|} \int_{\mathrm{BZ}'} dk\, G_{\alpha\beta\sigma}(k;z,z') \tag{9}$$

defines the local Green's function. The e-e scattering may thus be overestimated compared to an actual quasi-1D system. Hence, one can expect that the 2Bloc approximation provides an upper bound for thermalization effects. We note that within the local approximation, which is qualitatively similar to dynamical mean-field theory [34,42,43], the system can fully thermalize at sufficiently long times, in the sense that the single-particle density matrix becomes identical to that of a thermal equilibrium system.

Switching to a matrix notation for the sublattice indices (and dropping the spin index), the equation of motion for the GF becomes

$$[\mathrm{i}\partial_z - \mathbf{h}^{\mathrm{MF}}(z)]\mathbf{G}(k;z,z') = \int_{\mathcal{C}} dz''\, \mathbf{\Sigma}(z,z'')\mathbf{G}(k;z'',z'). \tag{10}$$

Projecting onto imaginary and real times and invoking the Langreth rules then yields the standard KBEs. The KBEs are solved using an in-house massively parallel computer code based on a fourth-order implicit predictor-corrector algorithm (similar to Ref. [63]). For the results presented in what follows, the time interval was split into $N_t = 3000$ equidistant points, while the imaginary branch (for the nonequilibrium calculations) was represented by $N_\tau = 800$ grid points. The Green's function for every k point has to be propagated simultaneously, which is accomplished by a distributed-memory layout. For obtaining converged results, we used $N_k = 256$ points in the reduced BZ.

III. LIGHT-CONTROLLED NONEQUILIBRIUM DYNAMICS OF THE CHARGE ORDER

The pseudospin representation (6) provides an intuitive picture for the control of CDWs by external fields. For instance, the asymmetric electronic charge on the sublattice sites can be switched with a single-cycle pulse (SCP) with a pulse duration T_p, see Fig. 1(a). During the pulse, the kinetic energy of the electrons with momentum k is shifted by the vector potential to $\epsilon_{k-A(t)}$. In the pseudospin picture, this acts as a momentum-dependent magnetic field in the z direction. In the weak-coupling regime, the major contribution to the CDW comes from the Fermi surface. Furthermore, $B^x_k(t)$ is smaller than the bandwidth and can be neglected during the pulse. Therefore, the CDW dynamics can be regarded as a spin precession around the z direction.

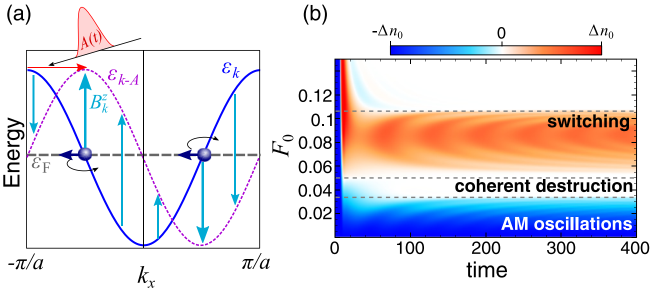

FIG. 1. (a) Schematic of the switching dynamics in the pseudospin picture (see text). A single-cycle field pulse shifts the noninteracting band structure, giving rise to a k-dependent effective magnetic field B^z_k. By tuning the precession time of the pseudospins, the dominant contribution arising from the Fermi level can be switched completely. (b) MF dynamics of the order parameter induced by a single-cycle pulse as a function of its amplitude F_0. The dashed lines separate the qualitatively different regimes.

By tuning the pulse amplitude and T_p we can control the pseudospins at the two Fermi points, which rotate in opposite directions [Fig. 1(a)]. Optimizing the pulse to induce a precession by $(2n+1)\pi$ $(n \in \mathbb{N})$, the sign of the order is switched. Inducing a rotation by $\frac{(2n+1)}{2}\pi$ $(n \in \mathbb{N})$, the pseudospin projections cancel out, which leads to an efficient destruction of the order. Note that the pseudospins at different k precess under a k-dependent pseudomagnetic field. Hence the complete pseudospin dynamics is subject to dephasing, which can reduce the size of the order parameter after the switching.

A. Mean-field dynamics

With this guidance, we proceed to the numerical investigation of the pulse-induced CDW dynamics. We propagated the MF Hamiltonian (6) in the presence of a SCP described by the electric field $E(t) = F_0 \sin^2[\pi(t-t_0)/T_\mathrm{p}]\sin[\omega(t-t_0)]$ with $T_\mathrm{p} = 2\pi/\omega$ [vector potential $A(t) = -\int_0^t dt' E(t')$]. We found that $T_\mathrm{p} = 13.6$ matches the typical timescale of the system and allows efficient switching as in the pseudospin picture. The SCPs considered here [64] have been realized in the optical regime [65,66].

In our MF study, we use the renormalized parameters $\tilde{J}_0 = 0.89 J_0$ and $\tilde{U} = 0.625U$. For this choice, the MF band structure provides a good approximation of the renormalized band structure resulting from including correlation effects, which is studied below. Details on this fitting procedure are presented in Appendix B. Employing these renormalized parameters allows us to use the MF dynamics as a reference for the correlated treatment below. In both cases, one obtains an equilibrium order parameter of $\Delta n_{\mathrm{eq}} \equiv -\Delta n_0 = -0.121$. The inverse temperature is fixed at $\beta = 40$.

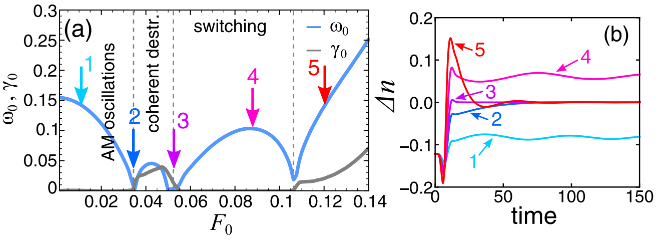

FIG. 2. (a) NEPD depicting the oscillation frequency ω_0 and damping constant γ_0 of the time-dependent order parameter. (b) Dynamics of $\Delta n(t)$ at the values of F_0 indicated in (a).

The MF dynamics of Δn for varying pulse strengths F_0 is presented in Fig. 1(b). Several regimes of qualitatively distinct dynamics can be identified (multiple dynamical phase transitions). For weak fields, the system exhibits persistent amplitude mode (AM) oscillations around a mean value $\Delta\bar{n}$. The corresponding frequency decreases with decreasing $|\Delta\bar{n}|$. The second regime corresponds to a rapid destruction of the CDW order. In particular, for $F_0 \simeq 0.05$ the order is almost immediately destroyed after the pulse, which is due to dephasing of the pseudospins and does not correspond to a thermal melting process. We therefore refer to this regime as coherent destruction (CD). Increasing F_0 further, the order is switched, as expected from the pseudospin picture. One observes the emergence of AM oscillations around the switched value. However, a complete switching is prevented by the dephasing of the pseudospins. The order parameter reaches an average value of $\Delta\bar{n} \simeq 0.66\Delta n_0$.

For a quantitative discussion of the different regimes, we analyze the dynamics by fitting the order parameter to the damped oscillating function $f(t) = c + [a\cos(\omega_0 t) + b\sin(\omega_0 t)]e^{-\gamma_0 t}$ in the long-time limit. This form describes (i) damped AM oscillations and (ii) nonoscillatory ($\omega_0 = 0$) decay of the order. The extracted damping constants γ_0 and oscillation frequencies ω_0 are presented in Fig. 2(a). The regime of AM oscillations is characterized by a finite ω_0 and a very small γ_0. A closer inspection reveals a very slow algebraic decay. The CD of the order is found in the region $0.035 < F_0 < 0.05$. It is bounded by two special points of slowing down at nonthermal critical points [43], where oscillations of the order parameter are fully suppressed [Fig. 2(b)]. In particular, at the right boundary $F_0 = 0.05$ the order is strongly suppressed already a short time after the pulse [the "sweet spot," marked as line 3 in Fig. 2(b)]. Within the CD regime, the system exhibits strongly damped AM oscillations after a rapid reduction of the mean value of Δn. Increasing the field strength further, the CDW system enters the switching regime. It is again characterized by AM oscillations, but around the switched value of the order parameter. For even larger pulse amplitude, the order is again destroyed and a second CD regime emerges.

B. Dynamics within the second-Born approximation

Now we consider the effect of scattering and thermalization processes on the NEPD. In general, the absorbed pulse energy (E_{abs}) will lead to a thermal melting of the order in the long-time limit in most scenarios.

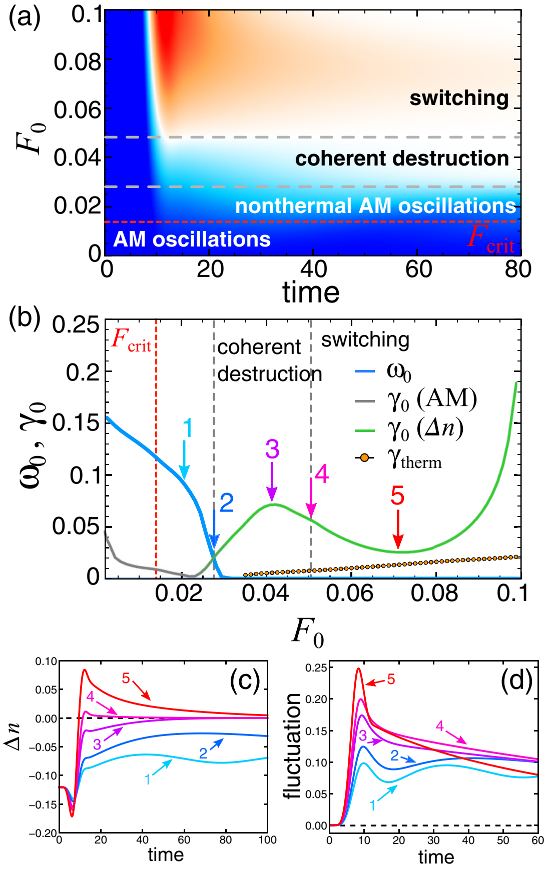

FIG. 3. (a) Pulse-induced 2Bloc dynamics of the order parameter as a function of pulse amplitude F_0. The dashed lines are analogous to Fig. 1(c). (b) Oscillation frequency ω_0 and damping constant γ_0 of the AMs (gray) or the nonoscillatory decay (green) of the order parameter. Also shown is the thermalization rate γ_{therm} extracted from $\mathcal{F}(t)$. (c) Order parameter for special values of F_0 as indicated in (b). (d) Fluctuation measure $\mathcal{F}(t)$ at the same values of F_0 as in (c).

Performing the analogous scan over the field strength F_0 with the same pulse shape as for the MF case yields the time-dependent order parameter and the NEPD presented in Figs. 3(a) and 3(b), respectively. Similarly to the MF case, the dynamics induced by the SCP exhibits qualitatively distinct regimes as F_0 is increased. For small amplitudes, the order parameter is subject to AM oscillations. Increasing the field strength, the total energy after the pump exceeds the energy of the equilibrium system at the critical temperature at the value $F_{\mathrm{crit}} \simeq 0.014$. Therefore, for $F > F_{\mathrm{crit}}$, one expects complete melting of the CDW after thermalization. Nevertheless, for $F_{\mathrm{crit}} < F_0 < 0.0275$ one finds long-lived AM oscillations with a small decay rate γ_0 [see Fig. 3(c)]. Such a persistence of nonthermal behavior over a long time span has also been observed in the dynamics of antiferromagnetic order [42,43].

As can be seen from the pseudospin equation of motion (6), the temporal change of the k-dependent contribution to the order parameter $\langle \hat{S}^x_{k\sigma}\rangle$ is proportional to $\langle \hat{S}^y_{k\sigma}\rangle$, i.e., it is proportional to the k-dependent current flowing between the sublattice sites. A genuine equilibrium situation is thus characterized not only by a vanishing total current, but by $\langle \hat{S}^y_{k\sigma}\rangle = 0$ for each k (no pseudospin precession). Conversely, a time dependence in $\langle \hat{S}^y_{k\sigma} \rangle$, even if the total sums up to zero, implies a nonequilibrium situation and thus a nonthermal state. To distinguish the effect of e-e scattering and thermalization from the effect of coherently precessing pseudospins, it is hence useful to introduce the fluctuation measure $\mathcal{F} \equiv (1/N_k)\sqrt{\sum_{k\sigma} |\langle \hat{S}^y_{k\sigma}\rangle|^2}$. As discussed above, this quantity provides a convenient measure of a nonthermal state: $\mathcal{F} = 0$ corresponds to thermal equilibrium, while $\mathcal{F} > 0$ indicates a nonequilibrium state. Progressing thermalization can be tracked by the decay of $\mathcal{F}(t)$. The nonthermal AM regime is thus characterized by an extremely slow thermalization, underpinned by the oscillating behavior of $\mathcal{F}(t)$ around a nonzero value [Fig. 3(d)].

For larger field strength, the order is destroyed rapidly, similarly as in the MF case. The CD is bounded by two special points: (i) a point of critical slowing-down at $F_0 \simeq 0.0275$, where the oscillation frequency approaches zero, and (ii) the "sweet spot" $F_0 \simeq 0.05$, where the CDW is rapidly destroyed. In contrast to the MF scenario, no (damped) AM oscillations occur; instead, a nonoscillatory decay of Δn is observed. The decay rate exhibits a maximum in the middle of the CD regime, similarly to the MF analysis. Since e-e collisions facilitate the suppression of the order, the CD regime is more extended. Note that the thermalization time is still rather long [Fig. 3(d)].

As in the MF analysis, a switching regime appears for larger field strengths, though the order decays due to scattering processes, leading to additional damping (and almost completely suppressed AM oscillations). This is due to the larger energy absorption, which acts against the CDW order. This is corroborated by the exponential decay of $\mathcal{F}(t)$ quantified by the thermalization rate γ_{therm} [shown in Fig. 3(b)]. Nevertheless, there is a pronounced minimum of the decay rate γ_0 at $F_0 \simeq 0.071$ in the middle of the switching regime. Here one encounters a nontrivial situation where, despite the increased E_{abs}, the relaxation of the order becomes slower (dynamical slowing-down). As the monotonic dependence of γ_{therm} shows, this slowdown is a nonthermal effect. It can be interpreted as a "trapping" in a state that is close to the MF transient state. A more detailed analysis also shows small oscillations on top of the exponential decay, which is reminiscent of the AM oscillations in the switching regime in Fig. 2(b).

C. Optimal control of CDW order

Now, we show how QOCT can stabilize nonthermal states further. In an optimal switching protocol, the requirements of minimal energy absorption and switching efficiency need to be balanced. Note that effectively noninteracting models neglect heating effects, in contrast to models which include e-e scattering. Using QOCT, we optimize the fields $A(t)$ to reach a target value of the order parameter, while simultaneously minimizing E_{abs}. Due to the substantial numerical cost, this procedure is applied only on the MF level. Since the MF dynamics is described by a nonlinear equation of motion for the one-body density matrix, the usual approach based on an (effective) Schrödinger equation (Krotov algorithm) is not applicable. In fact, one has to resort to gradient-free optimization methods because the derivative with respect to the driving field cannot be obtained analytically.

One might expect that pulses containing a minimal amount of field energy, as required to minimize heating effects, are relatively smooth functions without strong variations. On the other hand, the search space has to be large enough to find good approximations to the optimal fields. For these reasons, we parametrize the vector potential by

$$A(t) = \sum_{i=1}^{N_b} c_i B_i(t), \tag{11}$$

where $B_i(t)$ are fourth-order B-splines with respect to the time interval $[t_0, t_0 + T_{\text{p}}]$. To ensure that the corresponding electric field $E(t) = -\dot{A}(t)$ is zero at the end points of the interval and make sure no momentum is transferred to the system $[A(t_0 + T_{\text{p}}) = A(t_0) = 0]$, the boundary coefficients are fixed by $c_1 = c_2 = c_{N_b - 1} = c_{N_b} = 0$.

For the switching scenario, we are interested in the long-time stable dynamics of $\Delta n(t)$. As is known from the analysis with respect to the single-cycle pulses, the amplitude mode oscillations are expected to be present around a switched value of the order parameter after time t_1. We thus perform a linear fit $\Delta n_{\text{fit}}(t) = a(t - t_1) + b$ to the dynamics of $\Delta n(t)$ after the pulse. We then require that (i) the mean value of the order, encoded in b, is maximal, while (ii) the average slope $|a|$ should be minimal. The condition (ii) is necessary for the long-time stability of the switched state to ensure no drift can occur at longer timescales. Similarly, for coherent destruction one requires $|b|$ to be minimal. Gathering the B-spline coefficients in the vector $\mathbf{c}$, the target functional for switching the order from $\Delta n(t = 0) < 0$ is given by

$$J_{\text{switch}}[\mathbf{c}] = -b + \epsilon_1 |a| + \epsilon_2 E_{\text{abs}}, \tag{12}$$

while we use

$$J_{\text{CD}}[\mathbf{c}] = |b| + \epsilon_1 |a| + \epsilon_2 E_{\text{abs}} \tag{13}$$

for achieving coherent destruction. Here, ϵ_1 is a penalty parameter for the slope, whereas ϵ_2 denotes the penalty with respect to the absorbed energy E_{abs}. In order to evaluate the functionals (12) or (13), one has to perform the time propagation up to a sufficiently large time $T_{\max}$ (we set $T_{\max} = 500$), and compute the fitting parameters a, b and the absorbed energy. This procedure depends on the parameters N_b, ϵ_1, ϵ_2 and the pulse duration T_{p}. More details and sample calculations are presented in Appendix C.

After identifying optimal pulses, we can then compare the MF and correlated dynamics. A result of this optimization procedure for switching the CDW is shown in Fig. 4(b). The short-time 2Bloc dynamics is well described by the MF approximation. As compared to the simple SCP [Fig. 4(a)], the switching efficiency is bigger ($\Delta\bar{n} \simeq 0.75\Delta n_0$). In the MF results, the small amplitude of the AM oscillations indicates the stability of the state.

It is interesting to analyze the switching dynamics in the pseudospin picture. While the SCP monotonically rotates the spins close to the Fermi points by π [Fig. 4(c)], the optimized pulse initially leads to a rotation in the opposite direction to the switching [Fig. 4(d)]. As the snapshots of the k-dependent pseudospin configuration demonstrate, this procedure partially compensates the dephasing and thus results in a better switching.

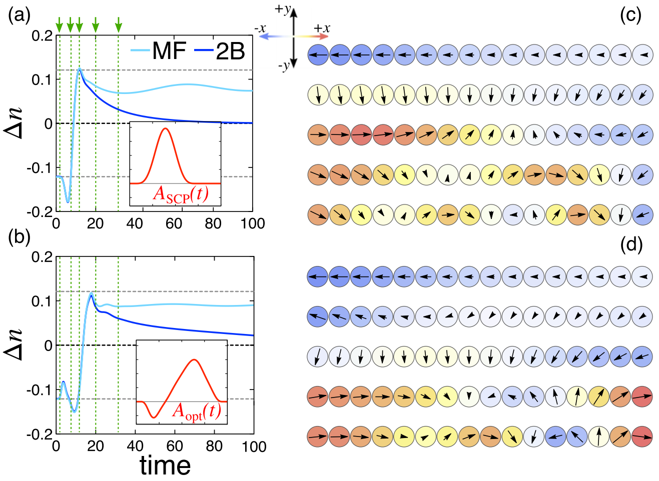

FIG. 4. Switching dynamics by a SCP (a) and optimized pulse (b). The inset depicts the respective vector potential $A(t)$. The pseudospin configuration for the time points marked with green arrows in the small range $[-0.5\pi/a,-0.4375\pi/a]$ close to the Fermi edge is shown for (c) the SCP and (d) the optimized pulse.

Including the e-e scattering, $\Delta n(t)$ exhibits damped behavior, whereas the short-time dynamics is well captured by the MF dynamics. Albeit E_{abs} exceeds the energy difference to the unordered state, the order parameter decays very slowly. Hence, the nonthermal flipped ordered state discussed in Fig. 3 is, due to minimizing E_{abs}, much more pronounced as compared to switching by the SCP. In fact, $\Delta n(t)$ shows more prominent oscillations on top of the decay for shorter times. Specifically, the pronounced shoulder right after the pulse indicates that the dynamics is close to the MF time evolution at short times. This is a clear signature of the switching regime in Fig. 1(c). Furthermore, the thermalization rate is reduced ($\gamma_{\mathrm{therm}}=0.0188$ for the SCP, $\gamma_{\mathrm{therm}}=0.0132$ for the optimized pulse).

Our method for optimizing the driving pulse can also be applied to the problem of rapid suppression of the CDW with minimal energy absorption. The pulse with the smallest E_{abs} is shown in Fig. 5(b) and compared to the dynamics driven by the SCP at the sweet spot [Fig. 5(a)] discussed in Sec. III. It is interesting to note that the simple single-cycle pulse results in a perfect suppression of the order while injecting only little energy into the system. Correspondingly, the optimized field $A(t)$ is qualitatively almost the same as the SCP. However, the absorbed energy is reduced such that the thermalization [Fig. 5(d)] is slower than for the SCP [Fig. 5(c)]. Even though after complete thermalization the system ends up in the disordered phase, the fluctuations decay on the very long timescale of $\gamma_{\mathrm{therm}}^{-1}\simeq 170$.

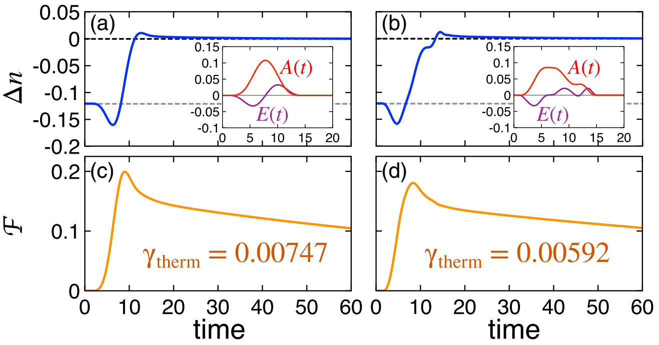

FIG. 5. Dynamics on the 2Bloc level at the sweet spot of coherent destruction: (a) single-cycle pulse and (b) optimized pulse. The insets show the laser fields. The corresponding fluctuation measure $\mathcal{F}(t)$ is shown in panels (c) and (d), respectively.

IV. DYNAMICS OF THE CHARGE ORDER IN THE HUBBARD-HOLSTEIN MODEL

So far, we have discussed the case of purely correlation-driven CDW order. In this section we extend the analysis to the situation where an e-ph coupling contributes to the CDW, with an emphasis on the following two points: (i) the robustness of the switching and coherent destruction dynamics presented in Sec. III, and (ii) the signatures of phonon- or correlation-driven charge order. Insight on the latter point provide a means of distinguishing e-e–from e-ph–driven CDW states.

To discuss these effects we extend the Hubbard model (1) to the Hubbard-Holstein model

$$\hat{H}(t)=\hat{H}_0(t)+\hat{H}_{\mathrm{e-e}}+\hat{H}_{\mathrm{e-ph}}+\hat{H}_{\mathrm{ph}}, \tag{14}$$

where the phonons are described by

$$\hat{H}_{\mathrm{ph}}=\omega_{\mathrm{ph}}\sum_{i,\alpha}\hat{b}^\dagger_{i\alpha}\hat{b}_{i\alpha}, \tag{15}$$

while the e-ph interaction is of the form

$$\hat{H}_{\mathrm{e-ph}}=g\sum_{i,\alpha,\sigma}\hat{n}_{i\alpha\sigma}\hat{X}_{i\alpha}. \tag{16}$$

Here, $\hat{X}_{i\alpha}=[\hat{b}^\dagger_{i\alpha}+\hat{b}_{i\alpha}]/\sqrt{2}$ represents the phonon distortion. The free part $[\hat{H}_0(t)]$ and the e-e interaction ($\hat{H}_{\text{e-e}}$) are the same as in Eq. (1). As thermalization effects are not the focus of the following discussion, we resort to the MF treatment of the Hamiltonian (14). This is accomplished by extending the effective single-particle Hamiltonian (2) to

$$\tilde{\mathbf{h}}^{\mathrm{MF}}(k,t)=\begin{pmatrix}\varepsilon_k(t) & \frac{g}{2}\Delta X(t)+\frac{U}{2}\Delta n(t)\\ \frac{g}{2}\Delta X(t)+\frac{U}{2}\Delta n(t) & \varepsilon_{k+Q}(t)\end{pmatrix}. \tag{17}$$

Here, $\Delta X(t)=\langle\hat{X}_{\mathrm{A}}(t)\rangle-\langle\hat{X}_{\mathrm{B}}(t)\rangle$ denotes the difference of the phonon amplitudes on the sublattice sites. To determine the self-consistent MF Hamiltonian (17), $\Delta X(t)$ also needs to be propagated. Combing the respective equations of motion of $\langle\hat{X}_{\mathrm{A,B}}(t)\rangle$, the distortion parameter is obtained from the equation

$$\frac{1}{2\omega_{\mathrm{ph}}}\left[\frac{d^2}{dt^2}+\omega_{\mathrm{ph}}^2\right]\Delta X(t)=-g\Delta n(t), \tag{18}$$

which we solve using the fourth-order Numerov method with the initial condition $\frac{d}{dt}\Delta X(t)=0$ for $t=0$.

In general, both the e-e and the e-ph coupling is responsible for the formation of the CDW. The combined contribution from

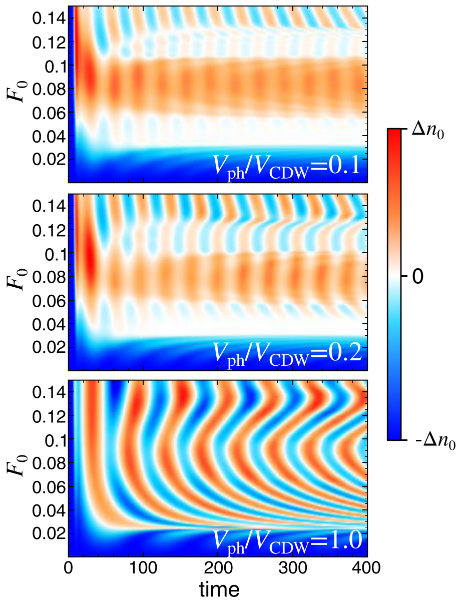

FIG. 6. Dynamics of the order parameter $\Delta n(t)$ induced by single-cycle pulses with strength F_0 [analogous to Fig. 1(b)] for different ratios of the contribution to the CDW from e-ph interactions (we fix $\omega_{\mathrm{ph}} = 0.2$).

both effects can be captured by the parameter

$$V_{\mathrm{CDW}} \equiv V_{\mathrm{ph}} + V_{\mathrm{e}} = \frac{g^2}{\omega_{\mathrm{ph}}} - \frac{U}{2}. \tag{19}$$

The parameter (19) is related to the interaction energy, as can be seen by computing the total energy in the MF approximation:

$$\begin{aligned} E_{\mathrm{tot}} &= 2\sum_k \mathrm{Tr}[\mathbf{h}^{(0)}(k)\boldsymbol{\rho}(k)] + \sum_k \mathrm{Tr}[(\mathbf{h}^{\mathrm{MF}}(k) - \mathbf{h}^{(0)}(k))\boldsymbol{\rho}(k)] \\ &\equiv E_0 + E_{\mathrm{int}}. \end{aligned}$$

Expressing the interaction energy by the order and distortion parameters in equilibrium, one finds $E_{\mathrm{int}} = -V_{\mathrm{CDW}}\Delta n^2$. Note that an identical value of V_{CDW}, regardless of the individual contributions of the e-e or e-ph interactions, gives rise to the same value of Δn and the gap size.

Fixing $V_{\mathrm{CDW}} = 0.625$ (corresponding to the results in Sec. III), we now vary the ratio $V_{\mathrm{ph}}/V_{\mathrm{CDW}}$ and study how the increased contribution of e-ph interactions to the order affects the pulse-induced dynamics. Figure 6 shows the nonequilibrium phase diagram analogous to Fig. 1(b) for $V_{\mathrm{ph}}/V_{\mathrm{CDW}} = 0.1$ (top), $V_{\mathrm{ph}}/V_{\mathrm{CDW}} = 0.2$ (middle), and $V_{\mathrm{ph}}/V_{\mathrm{CDW}} = 1$ (bottom). For a CDW dominated by e-e correlation effects, the different regimes of amplitude mode oscillations, coherent destruction, and switching are qualitatively still present, but superimposed with coherent phonon oscillations. It is interesting to see that the lower boundary of the coherent destruction regime represents the fastest way to destroy the order, whereas the sweet spot is exhibiting more oscillations. In general, the amplitude of the phonon oscillations increases under stronger driving.

The qualitative behavior of the laser-driven nonequilibrium regimes is still present for $V_{\mathrm{ph}}/V_{\mathrm{CDW}} = 0.2$, albeit the boundaries are smeared out by the phonon oscillations. For an even larger contribution of the electron-phonon coupling, the dynamics is dominated by the phonons and thus displays the generic behavior of the purely phonon-driven case (bottom panel in Fig. 6). In this scenario, the persistent oscillations of Δn with frequency ω_{ph} are the dominating feature. Neither destruction nor switching of the CDW is possible anymore. Similar nonequilibrium phases have been observed in experiments [18].

We conclude that a qualitatively different dynamics of the order parameter for different pulse amplitudes is a clear signature of a predominantly correlation-driven CDW formation. Weak e-ph coupling leads to small additional coherent phonon oscillations but does not suppress the characteristic features discussed in Sec. III. A larger contribution of the phonons, on the other hand, suppresses any switching behavior. This effect can be understood intuitively in the pseudospin representation: the role of the phonon can be regarded as a slowly changing magnetic field along the x direction. Therefore, B_k^x does not change even when the pseudospin rotates by $(2n+1)\pi$ ($n \in \mathbb{N}$), which makes the switched state unstable.

V. CONCLUSIONS

In summary, we revealed the rich *nonequilibrium phase diagram* of correlation-driven CDWs after laser excitation, which includes nonthermal AM oscillations, a sweet spot of rapid destruction of the order, a dynamical slowdown of the decay in the switching regime and hence multiple dynamical phase transitions. These features are well explained by the MF treatment and rationalized by the pseudospin picture and persist when e-e scattering effects are considered. The ability to switch the order or to completely suppress it is a fingerprint of correlation-driven CDWs; hence the transient dynamics allows us to identify the mechanism underlying the CDW. Tracing the predicted charge dynamics directly by inelastic x-ray scattering [67] is an interesting perspective for future experiments. Furthermore, the model can directly be implemented in cold atom setups, where our predictions can also be tested. Furthermore, QOCT allows us to identify optimal pulses for switching or melting of the order. Minimizing the absorbed energy delays the thermalization and may enable the emergence of competing orders on intermediate timescales. Controlled access to long-lived transient states has already resulted in technological applications [68], and we believe that our approach to QOCT can be usefully applied to the manipulation of a broad range of electronic orders.

ACKNOWLEDGMENTS

The calculations have been performed on the Beo04 cluster at the University of Fribourg and the Piz Daint cluster at the Swiss National Supercomputing Centre. This work has been supported by the Swiss National Science Foundation through NCCR MARVEL and ERC Consolidator Grant No. 724103. We thank Denis Golež for fruitful discussions.

APPENDIX A: BASIS REPRESENTATION

The basis with respect to the A, B sublattice sites (ss) in the extended unit cell is particularly convenient for introducing

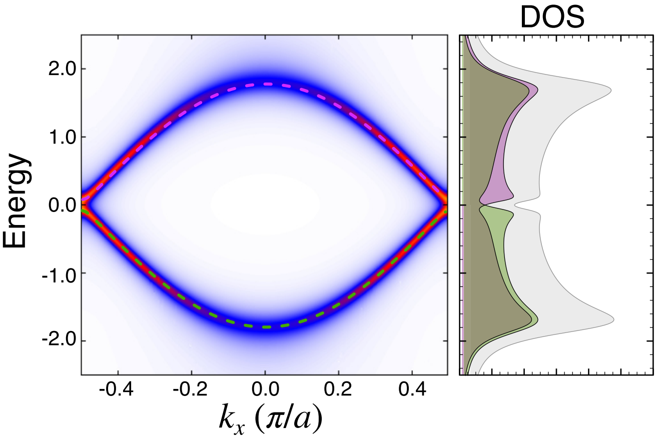

FIG. 7. Left panel: Spectral function $A(k,\omega)$ (summed over bands) within the 2Bloc approximation. The dashed lines represent the fit by the MF model with renormalized parameters $\widetilde{J}_0$ and $\widetilde{U}$. Right panel: Band-resolved (green and purple filled curves) and total (gray filled curve) density of states within the 2Bloc approximation. The parameters are, as in the main text, $U = -2$, $\beta = 40$.

approximations to the e-e interaction. These were exploited in Sec. II B, i.e., all calculations have been performed in the sublattice representation. An equivalent basis—which has been used to introduce the MF treatment in Sec. II A—is given by the momentum pair $(k, k+Q)$ with the nesting vector $Q = \pi/a$. The momentum-pair (mp) representation is most useful for defining pseudospin operators, as introduced in Sec. II A. Any k-dependent matrix in th ss representation ($\mathbf{A}_k$) can be transformed to the mp basis by the unitary transformation

$$\mathbf{A}_k^{(\mathrm{mp})} = \mathbf{R}_k \mathbf{A}_k^{(\mathrm{ss})} \mathbf{R}_k^\dagger \tag{A1}$$

with

$$\mathbf{R}_k = \frac{1}{\sqrt{2}} \begin{pmatrix} e^{ika/2} & e^{-ika/2} \\ e^{ika/2} & -e^{-ika/2} \end{pmatrix}. \tag{A2}$$

APPENDIX B: EQUILIBRIUM SPECTRAL FUNCTION AND MEAN-FIELD FIT

Before the KBEs can be solved (see Sec. II B), the equilibrium (Matsubara) Green's function needs to be computed. To this end, we solve the corresponding Dyson equation

$$\begin{aligned}\mathbf{G}(k;\tau) = \mathbf{g}(k;\tau) + \int_0^\beta d\tau' \int_0^\beta d\tau''\, \mathbf{g}(k;\tau-\tau') \\ \times \mathbf{\Sigma}(\tau'-\tau'')\mathbf{G}(k;\tau'').\end{aligned} \tag{B1}$$

Here, $\mathbf{g}(k,\tau)$ denotes the MF Green's function, while $\mathbf{\Sigma}(\tau)$ is the self-energy in the 2Bloc approximation. The Dyson equation (B1) is solved by a combination of Fourier transformation and fifth-order fixed-point iteration to improve the accuracy. A description of the method can be found in Ref. [69]. In the nonequilibrium calculations, we use $N_k = 256$ k points.

The spectral function $\mathbf{A}(k,\omega)$ in real-frequency space is obtained by Padé analytic continuation as in Ref. [69]. The band-integrated spectral function $A(k,\omega) = \sum_\alpha A_{\alpha\alpha}(k;\omega)$ is shown in Fig. 7. In accordance with the Luttinger-Ward theorem, the broadening due to many-body effects is least pronounced in the vicinity of the chemical potential $\mu = 0$, while significant broadening is apparent at the band top and bottom. Since we are in the weak-coupling regime, the main effect of the electronic correlations is a renormalization of the bands.

In order to be able to directly compare the dynamics within the MF and 2Bloc approximation, the band renormalization is taken into account in the effective parameters of the MF Hamiltonian (6) by replacing $J_0 \rightarrow \widetilde{J}_0$ and $U \rightarrow \widetilde{U}$. These parameters were determined by fitting the MF band structure to the maximum (with respect to ω) of $A(k,\omega)$, while requiring the order parameter to be identical (see Fig. 7). The result is $\widetilde{J}_0 = 0.89 J_0$ and $\widetilde{U} = 0.625 U$. The good quality of the fit is supported by the almost identical short-time dynamics within the MF and 2Bloc approximation, ensuring that applying the QOCT on the MF level provides optimal pulses for the correlated dynamics, as well.

APPENDIX C: PULSE OPTIMIZATION BY QUANTUM OPTIMAL CONTROL

The pulse optimization with the aim of switching or suppressing the CDW is based on the minimization of the target functionals (12) and (13), respectively. For their evaluation at the MF level, the time propagation of the nonlinear MF equations of motion has to be performed. Hence, the gradient with respect to the parameters **c** defining the pulse [cf. Eq. (11)] cannot be calculated directly. This is a significant complication as compared to the standard QOCT applied to the time-dependent Schrödinger equations, as in, for instance, Ref. [29]. Therefore, we minimize the functionals by a combination of the Pikaia genetic algorithm [70] for finding local minima and the NEWUOA algorithm [71] for finding the global minimum.

As explained in Sec. III C, the pulse optimization depends on the number of B-spline coefficients N_b, the slope penalty ϵ_1, the penalty with respect to the absorbed energy ϵ_2, and the pulse duration T_p. We performed the pulse optimization for various combinations of these parameters and found that $N_b = 28$ is enough to find the optimal pulse shapes. Increasing N_b yields essentially the same pulses with extra oscillations on top. Furthermore, the value of ϵ_1 affects the pulses only weakly, since most of the resulting pulses result in a vanishing average slope of $\Delta n(t)$. The pulse length T_p was varied from $T_\mathrm{p} = 5.0$ to $T_\mathrm{p} = 20.0$; we select the best pulses in this range for a fixed value of ϵ_2.

The energy penalty ϵ_2 is the most crucial parameter. Choosing $\epsilon_2 = 0$ results in very strong pulses, leading to almost perfect switching on the MF level [Fig. 8(a)]. However, within the 2Bloc approximation, the huge amount of absorbed energy rapidly destroys the order. Further analysis shows that the system thermalizes at a very high effective temperature shortly after the pulse. Gradually increasing ϵ_2 decreases the switching efficiency [Figs. 8(b)–8(f)] while reducing the energy absorption. This leads to a longer lifetime of the switched state within the 2Bloc dynamics. Interestingly, the shape of the vector potential $A(t)$ looks quite similar in Figs. 8(d)–8(f). It corresponds to the minimization of dephasing, which is explained in the main text. The best compromise between energy absorption and switching is provided by the pulse in Fig. 8(f). We found that applying a smoothing low-pass filter

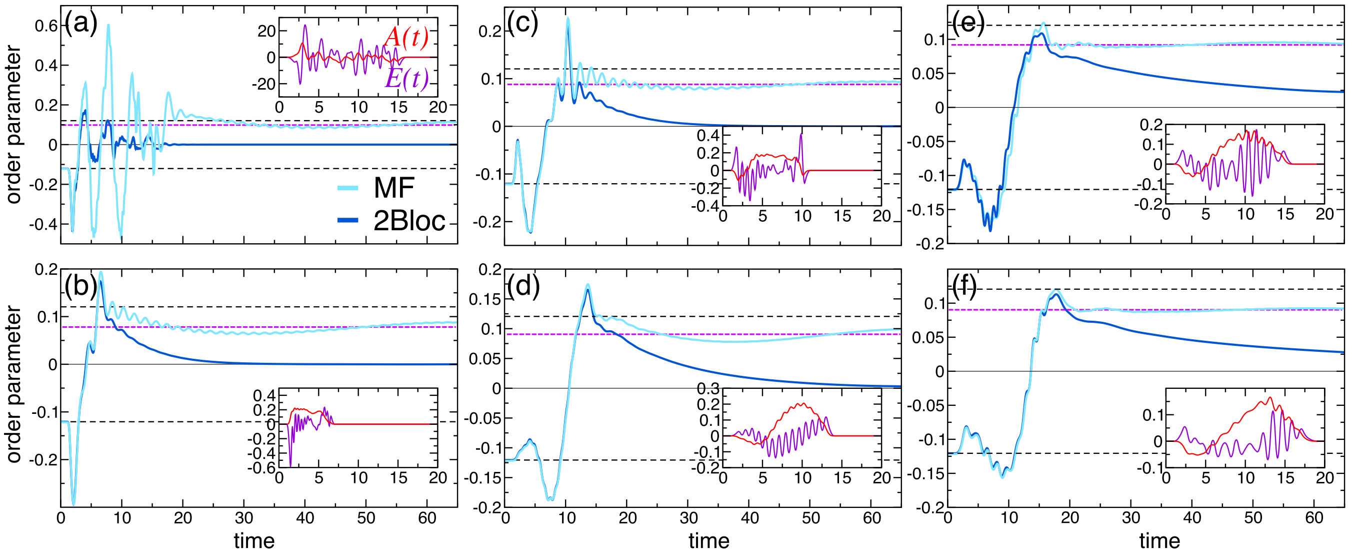

FIG. 8. Switching dynamics of the CDW order parameter induced by selected optimized pulses in the MF (light blue) and 2Bloc (dark blue) approximation. Panels (a)–(f) correspond to increasing energy penalty ϵ_2; in (a) $\epsilon_2 = 0$. The black dashed lines indicate the initial and flipped value $\pm\Delta n_0$, while the purple short-dashed lines represent the mean value $\Delta\bar{n}$ within the MF approximation.

further reduces E_{abs}, while the short-time dynamics is not altered. This optimal pulse is the one presented and discussed in the main text. Note that increasing ϵ_2 further leads to a suppression of switching, since the requirement to minimize the absorbed energy, which is zero if no pulse is applied, starts to dominate.

APPENDIX D: ANISOTROPIC TWO-DIMENSIONAL LATTICE

In the main text, we consider a one-dimensional configuration of the lattice. Note that the local approximation to the self-energy leads to generic features of a higher-dimensional system, while the 1D character primarily enters via the free band structure. Most CDW orders observed in materials are, in fact, 2D (typically stripe or checkerboard order). In this section we confirm that our results based on the 1D system are also valid for the 2D case with anisotropic hopping. To be specific, we consider a square lattice with hopping J_0 in the x direction and $(1-\delta)J_0$ in the y direction [see Fig. 9(a)]; $\delta = 0$ corresponds to the isotropic 2D system, while $\delta = 1$ recovers the 1D limit. The CDW forming in this configuration follows a checkerboard order, corresponding to a nesting vector $\mathbf{Q} = (\pi/a,\pi/a)$.

The treatment from Sec. II is applicable to the 2D case as well, after (i) replacing the 1D wave vector k by a vector $\mathbf{k}$ from the reduced Brillouin zone shown in Fig. 9(b), and (ii) modifying the free Hamiltonian [with respect to the momentum-pair basis $(\mathbf{k},\mathbf{k}+\mathbf{Q})$] to

$$\mathbf{h}^{(0)}(\mathbf{k}) = \begin{pmatrix} \varepsilon(\mathbf{k}) & \frac{U}{2}\Delta n \\ \frac{U}{2}\Delta n & \varepsilon(\mathbf{k}+\mathbf{Q}) \end{pmatrix}. \tag{D1}$$

Here,

$$\varepsilon(\mathbf{k}) = -2J_0[\cos(k_x a) + (1-\delta)\cos(k_y a)] \tag{D2}$$

denotes the original free band structure.

We have performed equilibrium calculations with the 2Bloc approximation for different values of δ [see Fig. 9(c)]. The order parameter Δn deviates by less than 10% from the 1D value in the regime of anisotropy $\delta = 0.7\ldots1$. This relatively large span shows that small deviations from our 1D setup have almost no influence on the results discussed in the main text.

Furthermore, we have analyzed the pulse-induced dynamics in the 2D scenario. As an example, we show the dynamics of the order parameter at the "sweet spot" of coherent destruction within the MF approximation in Fig. 9(d). We applied the same pulse as for the 1D case (polarization along the x direction). One observes similar behavior as for the equilibrium

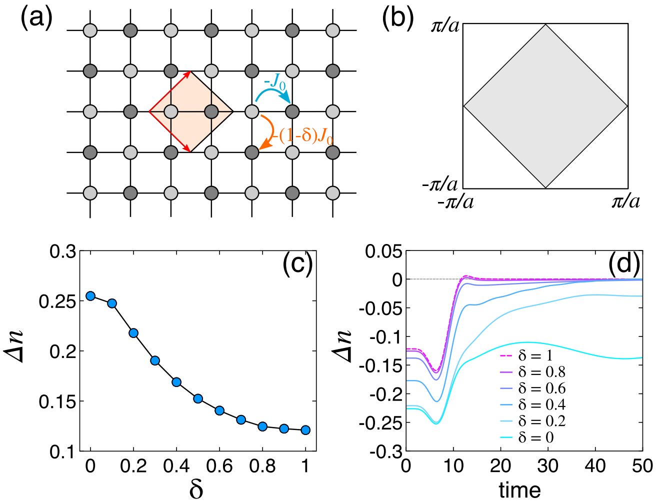

FIG. 9. (a) Sketch of the checkerboard CDW order in an anisotropic 2D square lattice. The shaded area shows the unit cell chosen for the calculations. (b) Full (white square) and reduced (gray shaded) Brillouin zone. (c) Dependence of the order parameter Δn on the anisotropy δ. (d) Dynamics induced by the single-cycle pulse at the point of coherent destruction for different values of δ.

properties: for moderately strong anisotropy, the time evolution of Δn is very close to the 1D case. Therefore, the different regimes of the nonequilibrium phase diagram discussed in the main text are also relevant for the anisotropic 2D system.

[1] R. Mankowsky, A. Subedi, M. Först, S. O. Mariager, M. Chollet, H. T. Lemke, J. S. Robinson, J. M. Glownia, M. P. Minitti, A. Frano, M. Fechner, N. A. Spaldin, T. Loew, B. Keimer, A. Georges, and A. Cavalleri, Nature (London) **516**, 71 (2014).

[2] S. Kaiser, C. R. Hunt, D. Nicoletti, W. Hu, I. Gierz, H. Y. Liu, M. Le Tacon, T. Loew, D. Haug, B. Keimer, and A. Cavalleri, Phys. Rev. B **89**, 184516 (2014).

[3] M. Mitrano, A. Cantaluppi, D. Nicoletti, S. Kaiser, A. Perucchi, S. Lupi, P. Di Pietro, D. Pontiroli, M. Riccò, S. R. Clark, D. Jaksch, and A. Cavalleri, Nature (London) **530**, 461 (2016).

[4] M. A. Sentef, A. F. Kemper, A. Georges, and C. Kollath, Phys. Rev. B **93**, 144506 (2016).

[5] D. M. Kennes, E. Y. Wilner, D. R. Reichman, and A. J. Millis, Nat. Phys. **13**, 479 (2017).

[6] M. Babadi, M. Knap, I. Martin, G. Refael, and E. Demler, Phys. Rev. B **96**, 014512 (2017).

[7] Y. Murakami, N. Tsuji, M. Eckstein, and P. Werner, Phys. Rev. B **96**, 045125 (2017).

[8] G. Mazza and A. Georges, Phys. Rev. B **96**, 064515 (2017).

[9] N. Bittner, T. Tohyama, S. Kaiser, and D. Manske, arXiv:1706.09366.

[10] E. Möhr-Vorobeva, S. L. Johnson, P. Beaud, U. Staub, R. De Souza, C. Milne, G. Ingold, J. Demsar, H. Schaefer, and A. Titov, Phys. Rev. Lett. **107**, 036403 (2011).

[11] D. Golež, P. Werner, and M. Eckstein, Phys. Rev. B **94**, 035121 (2016).

[12] S. Mor, M. Herzog, D. Golež, P. Werner, M. Eckstein, N. Katayama, M. Nohara, H. Takagi, T. Mizokawa, C. Monney, and J. Stähler, Phys. Rev. Lett. **119**, 086401 (2017).

[13] Y. Murakami, D. Golež, M. Eckstein, and P. Werner, Phys. Rev. Lett. **119**, 247601 (2017).

[14] H. Okamoto, K. Ikegami, T. Wakabayashi, Y. Ishige, J. Togo, H. Kishida, and H. Matsuzaki, Phys. Rev. Lett. **96**, 037405 (2006).

[15] S. D. Conte, L. Vidmar, D. Golež, M. Mierzejewski, G. Soavi, S. Peli, F. Banfi, G. Ferrini, R. Comin, B. M. Ludbrook, L. Chauviere, N. D. Zhigadlo, H. Eisaki, M. Greven, S. Lupi, A. Damascelli, D. Brida, M. Capone, J. Bonča, G. Cerullo, and C. Giannetti, Nat. Phys. **11**, 421 (2015).

[16] A. Cavalleri, D. Polli, G. Cerullo, M. Rini, R. W. Schoenlein, S. Wall, Y. Tokura, and Y. Tomioka, Nat. Mater. **6**, 643 (2007).

[17] K. Onda, S. Ogihara, K. Yonemitsu, N. Maeshima, T. Ishikawa, Y. Okimoto, X. Shao, Y. Nakano, H. Yamochi, G. Saito, and S.-Y. Koshihara, Phys. Rev. Lett. **101**, 067403 (2008).

[18] T. Huber, S. O. Mariager, A. Ferrer, H. Schäfer, J. A. Johnson, S. Grübel, A. Lübcke, L. Huber, T. Kubacka, C. Dornes, C. Laulhe, S. Ravy, G. Ingold, P. Beaud, J. Demsar, and S. L. Johnson, Phys. Rev. Lett. **113**, 026401 (2014).

[19] W. Shen, Y. Ge, A. Y. Liu, H. R. Krishnamurthy, T. P. Devereaux, and J. K. Freericks, Phys. Rev. Lett. **112**, 176404 (2014).

[20] A. Caviezel, A. Ferrer, A. Robert, C. Dornes, D. Zhu, G. Ingold, H. T. Lemke, H. Wadati, J. A. Johnson, J. M. Glownia, L. Rettig, M. Chollet, M. Kawasaki, M. Nakamura, M. Radovic, M. Sikorski, P. Beaud, S.-W. Huang, S. L. Johnson, S. O. Mariager *et al.*, Nat. Mater. **13**, 923 (2014).

[21] A. Cavalleri, T. Dekorsy, H. H. W. Chong, J. C. Kieffer, and R. W. Schoenlein, Phys. Rev. B **70**, 161102 (2004).

[22] M. Chollet, L. Guerin, N. Uchida, S. Fukaya, H. Shimoda, T. Ishikawa, K. Matsuda, T. Hasegawa, A. Ota, H. Yamochi, G. Saito, R. Tazaki, S.-I. Adachi, and S.-Y. Koshihara, Science **307**, 86 (2005).

[23] S. Iwai, K. Yamamoto, A. Kashiwazaki, F. Hiramatsu, H. Nakaya, Y. Kawakami, K. Yakushi, H. Okamoto, H. Mori, and Y. Nishio, Phys. Rev. Lett. **98**, 097402 (2007).

[24] R. V. Yusupov, T. Mertelj, J.-H. Chu, I. R. Fisher, and D. Mihailovic, Phys. Rev. Lett. **101**, 246402 (2008).

[25] M. Porer, U. Leierseder, J.-M. Ménard, H. Dachraoui, L. Mouchliadis, I. E. Perakis, U. Heinzmann, J. Demsar, K. Rossnagel, and R. Huber, Nat. Mater. **13**, 857 (2014).

[26] K. Yonemitsu and N. Maeshima, Phys. Rev. B **76**, 075105 (2007).

[27] H. Hashimoto, H. Matsueda, H. Seo, and S. Ishihara, J. Phys. Soc. Jpn. **83**, 123703 (2014).

[28] O. P. Matveev, A. M. Shvaika, T. P. Devereaux, and J. K. Freericks, Phys. Rev. B **94**, 115167 (2016).

[29] B. Hwang and P. M. Duxbury, Phys. Rev. A **94**, 043404 (2016).

[30] Y. Wang, B. Moritz, C.-C. Chen, C. J. Jia, M. van Veenendaal, and T. P. Devereaux, Phys. Rev. Lett. **116**, 086401 (2016).

[31] H. Hashimoto and S. Ishihara, Phys. Rev. B **96**, 035154 (2017).

[32] Y. Kamihara, H. Hiramatsu, M. Hirano, R. Kawamura, H. Yanagi, T. Kamiya, and H. Hosono, J. Am. Chem. Soc. **128**, 10012 (2006).

[33] D. Fausti, R. I. Tobey, N. Dean, S. Kaiser, A. Dienst, M. C. Hoffmann, S. Pyon, T. Takayama, H. Takagi, and A. Cavalleri, Science **331**, 189 (2011).

[34] M. Eckstein, M. Kollar, and P. Werner, Phys. Rev. Lett. **103**, 056403 (2009).

[35] M. Heyl, Phys. Rev. Lett. **113**, 205701 (2014).

[36] B. Žunkovič, M. Heyl, M. Knap, and A. Silva, Phys. Rev. Lett. **120**, 130601 (2018).

[37] E. A. Yuzbashyan and M. Dzero, Phys. Rev. Lett. **96**, 230404 (2006).

[38] R. A. Barankov and L. S. Levitov, Phys. Rev. Lett. **96**, 230403 (2006).

[39] F. Peronaci, M. Schiró, and M. Capone, Phys. Rev. Lett. **115**, 257001 (2015).

[40] G. Mazza, Phys. Rev. B **96**, 205110 (2017).

[41] M. Schiró and M. Fabrizio, Phys. Rev. Lett. **105**, 076401 (2010).

[42] P. Werner, N. Tsuji, and M. Eckstein, Phys. Rev. B **86**, 205101 (2012).

[43] N. Tsuji, M. Eckstein, and P. Werner, Phys. Rev. Lett. **110**, 136404 (2013).

[44] M. Marcuzzi, J. Marino, A. Gambassi, and A. Silva, Phys. Rev. Lett. **111**, 197203 (2013).

[45] A. Lerose, J. Marino, B. Žunkovič, A. Gambassi, and A. Silva, Phys. Rev. Lett. **120**, 130603 (2018).

[46] B. Sciolla and G. Biroli, Phys. Rev. Lett. **105**, 220401 (2010).

[47] R. Eitan, M. Mundt, and D. J. Tannor, Phys. Rev. A **83**, 053426 (2011).

[48] D. M. Reich, M. Ndong, and C. P. Koch, J. Chem. Phys. **136**, 104103 (2012).

[49] R. Schmidt, A. Negretti, J. Ankerhold, T. Calarco, and J. T. Stockburger, Phys. Rev. Lett. **107**, 130404 (2011).

[50] A. Toschi, P. Barone, M. Capone, and C. Castellani, New J. Phys. **7**, 7 (2005).

[51] M. A. Sentef, A. Tokuno, A. Georges, and C. Kollath, Phys. Rev. Lett. **118**, 087002 (2017).

[52] D. Greif, T. Uehlinger, G. Jotzu, L. Tarruell, and T. Esslinger, Science **340**, 1307 (2013).

[53] R. A. Hart, P. M. Duarte, T.-L. Yang, X. Liu, T. Paiva, E. Khatami, R. T. Scalettar, N. Trivedi, D. A. Huse, and R. G. Hulet, Nature (London) **519**, 211 (2015).

[54] A. Mazurenko, C. S. Chiu, G. Ji, M. F. Parsons, M. Kanász-Nagy, R. Schmidt, F. Grusdt, E. Demler, D. Greif, and M. Greiner, Nature (London) **545**, 462 (2017).

[55] F. Görg, M. Messer, K. Sandholzer, G. Jotzu, R. Desbuquois, and T. Esslinger, Nature (London) **553**, 481 (2018).

[56] Estimating $J_0 \approx 1$ eV, the unit of time is ∼4.1 fs.

[57] A. Alvermann and H. Fehske, J. Comput. Phys. **230**, 5930 (2011).

[58] P. W. Anderson, Phys. Rev. **112**, 1900 (1958).

[59] R. Matsunaga, N. Tsuji, H. Fujita, A. Sugioka, K. Makise, Y. Uzawa, H. Terai, Z. Wang, H. Aoki, and R. Shimano, Science **345**, 1145 (2014).

[60] M. A. Sentef, M. Claassen, A. F. Kemper, B. Moritz, T. Oka, J. K. Freericks, and T. P. Devereaux, Nat. Commun. **6**, 7047 (2015).

[61] K. Balzer and M. Bonitz, *Nonequilibrium Green's Functions Approach to Inhomogeneous Systems* (Springer, New York, 2012).

[62] G. Stefanucci and R. V. Leeuwen, *Nonequilibrium Many-Body Theory of Quantum Systems: A Modern Introduction* (Cambridge University Press, Cambridge, UK, 2013).

[63] M. Schüler, J. Berakdar, and Y. Pavlyukh, Phys. Rev. B **93**, 054303 (2016).

[64] In SI units, the peak intensity of the strongest pulse considered here is $I_0 \approx 5 \times 10^{14}$ W cm^2 (assuming a lattice constant $a \approx 4$ Å). Estimating the hopping $J_0 \approx 1$ eV, the pulse duration is $T_\mathrm{p} \approx 56$ fs.

[65] D. You, D. R. Dykaar, R. R. Jones, and P. H. Bucksbaum, Opt. Lett. **18**, 290 (1993).

[66] E. Goulielmakis, M. Schultze, M. Hofstetter, V. S. Yakovlev, J. Gagnon, M. Uiberacker, A. L. Aquila, E. M. Gullikson, D. T. Attwood, R. Kienberger, F. Krausz, and U. Kleineberg, Science **320**, 1614 (2008).

[67] K. Iwano, Phys. Rev. Lett. **102**, 106405 (2009).

[68] I. Vaskivskyi, J. Gospodaric, S. Brazovskii, D. Svetin, P. Sutar, E. Goreshnik, I. A. Mihailovic, T. Mertelj, and D. Mihailovic, Sci. Adv. **1**, e1500168 (2015).

[69] M. Schüler and Y. Pavlyukh, Phys. Rev. B **97**, 115164 (2018).

[70] P. Charbonneau, Astrophys. J., Suppl. Ser. **101**, 309 (1995).

[71] G. Pillo and M. Roma, *Large-Scale Nonlinear Optimization* (Springer Science & Business Media, New York, 2006).